Research Square

Preprints are preliminary reports that have not undergone peer review.
They should not be considered conclusive, used to inform clinical practice,
or referenced by the media as validated information.

Coronary Urate Detected by Spectral CT Marks the Vulnerable Plaque

Shinichiro Fujimoto

snfujimo@juntendo.ac.jp

Juntendo University Graduate School of Medicine https://orcid.org/0000-0002-7648-1977

Hideyuki Sato

Department of Radiological Technology, Juntendo University Hospital

Yuko Kawaguchi

Department of Cardiovascular Biology and Medicine, Juntendo University Graduate School of Medicine

Lili Száraz

Department of Radiology, Medical Imaging Centre, Semmelweis University

Tatsuya Shiraki

CVPath Institute https://orcid.org/0000-0003-1901-1642

Nobuo Tomizawa

Juntendo University Graduate School of Medicine https://orcid.org/0000-0001-6305-1081

Yui Nozaki

Department of Cardiovascular Biology and Medicine, Juntendo University Graduate School of Medicine

Yosuke Kogure

Department of Radiological Technology, Juntendo University Hospital

Kensuke Nishimiya

Department of Pathology and Cardiovascular Institute, Mass General Brigham and Harvard Medical School

Craig Cassidy

Heart and Vascular Institute and Department of Pathology, McGovern Medical School, University of Texas Health Science Centre

Navneet Narula

Heart and Vascular Institute and Department of Pathology, McGovern Medical School, University of Texas Health Science Centre

Attila Fintha

Department of Pathology and Experimental Cancer Research, Semmelweis University

Filippo Cademartiri

University of Montreal

Guillermo Tearney

Department of Pathology and Cardiovascular Institute, Mass General Brigham and Harvard Medical School

Aloke Finn
CVPath Institute

Jasvinder Singh
Division of Rheumatology, Baylor College of Medicine

Thomas Lüscher
Royal Brompton and Harefield Hospitals, Imperial College and King's College London

Jean-Claude Tardif
Montreal Heart Institute https://orcid.org/0000-0002-8200-8983

Renu Virmani
CVPath Institute

Pál Maurovich-Horvat
Department of Radiology, Medical Imaging Centre, Semmelweis University

Tohru Minamino
Juntendo University Graduate School of Medicine

Jagat Narula
University of Texas

Article

Keywords:

Posted Date: October 6th, 2026

DOI: https://doi.org/10.21203/rs.3.rs-11199818/v1

License: This work is licensed under a Creative Commons Attribution 4.0 International License.
Read Full License

Additional Declarations: Yes there is potential Competing Interest. J.S.has received consultant fees from ROMTech, Atheneum, Clearview healthcare partners, Yale, Hulio, Horizon Pharmaceuticals/DINORA, ANI/Exeltis, USA Inc., Frictionless Solutions, Schipher, Crealta/Horizon, Medisys, Fidia, PK Med, Two labs Inc., Adept Field Solutions, Clinical Care options, Putnam associates, Focus forward, Navigant consulting, Spherix, MedIQ, Jupiter Life Science, UBM LLC, Trio Health, Medscape, WebMD, and Practice Point communications; the National Institutes of Health; and the American College of Rheumatology. J.S. has received institutional research support from Zimmer Biomet Holdings. J.S. received food and beverage payments from Intuitive Surgical Inc./Philips Electronics North America. J.S. owns stock options in Atyr pharmaceuticals, Atai life sciences, Kintara Therapeutics, Intelligent Biosolutions, Acumen pharmaceutical, TPT Global Tech, Vaxart pharmaceuticals, Atyu biopharma, Adaptimmune Therapeutics, GeoVax Labs, Pieris Pharmaceuticals, Enzolytics Inc., Seres Therapeutics, Tonix

Pharmaceuticals Holding Corp., Aebona Pharmaceuticals, and Charlotte's Web Holdings, Inc. J.S. previously owned stock options in Amarin, Viking and Moderna pharmaceuticals. J.S. was on the speaker's bureau of Simply Speaking. J.S. was a member of the executive of Outcomes Measures in Rheumatology (OMERACT), an organization that develops outcome measures in rheumatology and receives arms-length funding from 8 companies. J.S. previously served on the FDA Arthritis Advisory Committee. J.S. previously served as a member of the following committees: member, the American College of Rheumatology's (ACR) Annual Meeting Planning Committee (AMPC) and Quality of Care Committees, the Chair of the ACR Meet-the-Professor, Workshop and Study Group Subcommittee and the co-chair of the ACR Criteria and Response Criteria subcommittee. J-C.T. has received research grants or research support from Amgen, Boehringer Ingelheim, Ceapro, DalCor Pharmaceuticals, Merck, Novartis, Novo Nordisk, and Verve Therapeutics. J-C.T. holds investments in DalCor Pharmaceuticals. J-C.T. has received personal compensation, including honoraria, consulting fees, advisory roles, or other professional income, from DalCor Pharmaceuticals, Merck, Pendopharm, and Zentiva. J-C.T. has been involved in intellectual property related to pharmacogenomics-guided CETP inhibition and the use of colchicine after myocardial infarction. J-C.T. has waived his rights to the colchicine patent and does not receive any financial benefit from it.

Abstract

Hyperuricaemia and gout predict cardiovascular events, yet whether urate acts within coronary plaque is unknown, and lowering serum urate has not reduced risk. Here, we show that non-contrast, ECG-gated dual-energy computed tomography identifies urate within coronary plaque and separates it from calcium, which single-energy CT cannot. Among 116 patients (348 vessels), coronary urate occurred in 35.3% of patients and 17.5% of vessels and was the only independent predictor of high-risk plaque (odds ratio 4.91; 95% confidence interval 1.43-16.82); the calcium score was not. Urate-positive patients were normouricaemic, indicating local deposition. In an independent cohort of 92 patients, photon-counting CT, using a different spectral mechanism, corroborated the finding from the routine calcium-scoring scan. Cross-polarised micro-optical coherence tomography confirmed needle-shaped, negatively birefringent monosodium urate crystals, and histopathology localised xanthine oxidase to $CD68^{+}$/CD163-low macrophages at the necrotic-core periphery, rising with plaque progression. Coronary urate is an imageable marker of crystal-driven inflammation and plaque vulnerability.

Introduction

Atherosclerosis is a chronic inflammatory disease, and a substantial burden of cardiovascular risk persists after guideline lipid targets are met[1]. Endogenous crystalline material is a potent driver of innate immunity: cholesterol crystals activate the NLRP3 inflammasome and are required for experimental atherogenesis[2], and the NLRP3-interleukin-1β (IL-1β) axis links such signals to plaque progression and instability[3]. Therapies that engage this axis reduce events independently of lipid lowering, establishing residual inflammatory risk as a bona fide therapeutic target. Yet the upstream, plaque-specific triggers that ignite the inflammasome within an individual lesion remain poorly defined and invisible on clinical imaging, so the inflammation-active plaque cannot, at present, be identified in a living patient. Whether a discrete, detectable crystalline trigger exists in the coronary wall, one that could be both imaged and therapeutically targeted, is unknown.

Hyperuricaemia and gout are consistently associated with excess cardiovascular events and mortality[4–5], an association that has resisted mechanistic explanation for decades. Monosodium urate (MSU) is the archetypal pro-inflammatory crystal, engaging NLRP3 in macrophages and neutrophils to release IL-1β and IL-18[6–7], and MSU together with xanthine oxidase (XO) has been recovered from human carotid endarterectomy specimens[8], hinting that urate can deposit within the arterial wall. The coronary arteries, however, where crystal-driven inflammation would be most consequential, have not been examined, and whether coronary MSU exists, how common it is, and whether it identifies the vulnerable plaque have not been established.

A central paradox has obscured this question. Circulating urate is an abundant plasma antioxidant, yet the xanthine-oxidase form of xanthine oxidoreductase is a powerful intracellular source of superoxide and hydrogen peroxide, coupling urate production to local oxidative stress[9]. The vascular consequences

of urate may therefore depend on where it is generated and deposited rather than on its circulating concentration, a distinction that would reconcile the epidemiological risk of gout and hyperuricaemia with the neutral cardiovascular results of serum urate-lowering trials.

Dual-energy CT resolves materials by their electron density and effective atomic number and differentiates uric acid from calcium-containing kidney stones and gout from calcium pyrophosphate disease[10–12]. Only isolated reports describe DECT-verified urate in the coronary vasculature, exclusively in patients with established gout[13–16]. Single-energy CT instead quantifies calcium as the Agatston score[17–19], but unstable plaques are frequently non- or minimally calcified[20–22], and increasing calcium density accompanies stabilisation rather than risk[23–25]; calcium therefore reports the burden of disease but not, on its own, its propensity to rupture. We reasoned that a spectral method capable of resolving a second, non-calcific crystalline species might reveal an inflammatory axis that calcium scoring misses. We therefore used non-contrast, ECG-gated DECT to detect coronary MSU, tested its association with CT-defined high-risk plaque, and sought validation along three orthogonal lines: photon-counting CT in a separate cohort, to establish that the signal is not an artefact of one spectral platform; multiplex histopathology of human coronary specimens to define the cellular and enzymatic origin of the crystal; and cross-polarised micro-optical coherence tomography, to confirm the physical crystal by an entirely non-radiographic contrast mechanism. Because the signature is obtained from a non-contrast acquisition, without contrast medium or radiotracer, a positive result would be immediately translatable to routine imaging.

Results

DECT discriminates monosodium urate from calcium in phantoms

On single-energy CT, monosodium urate is a wolf in calcium's clothing. In an electron-density phantom scanned at 120 kVp, the MSU rod attenuated at 308.9 HU, far above the 130 HU threshold that defines *calcium* for Agatston scoring, and essentially identical to intermediate-density calcium (50, 100 and 300 mg mL^{-1} calcium measured 200.7, 340.2 and 897.1 HU; adipose −64.1 HU). Attenuation alone, therefore, cannot tell the two apart. Dual-energy analysis broke the tie through two physically independent parameters. The effective atomic number of MSU (8.4) fell distinctly below that of calcium (9.7 at 100 mg mL^{-1}, rising to 12.1 at 300 mg mL^{-1}) and above that of adipose (6.0), while its electron density (4.3 × 10^{23} electrons cm^{-3}) lay between low- and high-concentration calcium (3.8-4.9 × 10^{23}). Two-material decomposition rendered MSU as a discrete overlay confined to the urate rod (Fig. 1). The combined electron-density and effective-atomic-number signature thus separates MSU cleanly from both calcium and lipid.

Coronary MSU is prevalent and dissociated from systemic urate

We then applied this signature in vivo, analysing non-contrast, ECG-gated DECT in 116 consecutive patients referred for suspected coronary artery disease (348 vessels; Table 1). The cohort was

unselected for urate status and, on average, normouricaemic (mean serum urate 5.2 ± 1.3 mg dL^{-1}). Coronary MSU was nonetheless not infrequent: it was detected in 41 of 116 patients (35.3%) and 61 of 348 vessels (17.5%; Fig. 2A-D). MSU-positive patients were more often male (73.2% vs 46.7%), hypertensive (70.7% vs 45.3%) and obese, carried a far higher calcium burden (median Agatston 302 vs 3) and had more obstructive disease (56.1% vs 12.0%; all $P < 0.05$; Table 2), while trending toward more diabetes (34.1% vs 20.0%, $P = 0.12$). Their serum urate was only marginally higher (5.7 ± 1.4 vs 4.9 ± 1.2 mg dL^{-1}), remained within the normouricaemic range, and overlapped extensively with that of MSU-negative patients. Coronary MSU is therefore not necessarily associated with gout but a common feature of coronary atherosclerosis and one that the blood test does not predict, pointing to local, intra-plaque crystallisation rather than resulting from a supersaturated circulation.

Coronary MSU independently predicts high-risk plaque

Although MSU-positive patients had numerically more high-risk plaque, the difference was not significant when patients were the unit of analysis (12.2% vs 6.7%, $P = 0.32$); the association with the vulnerable phenotype emerged when individual vessels were examined. This suggests that a patient may harbour one crystal-bearing, inflammation-active plaque among two otherwise quiescent arteries, so patient-level averaging dilutes the signal of interest. It also indicates that coronary MSU is not a systemic trait expressed uniformly throughout the coronary tree, but a property of lesions, the unit at which rupture occurs.

Coronary MSU tracked the vulnerable phenotype rather than mere disease burden. At the vessel level, MSU-positive vessels were far more likely to show low-attenuation plaque (11.5% vs 3.1%), positive remodelling (18.0% vs 5.2%), spotty calcification (44.3% vs 22.0%) and composite high-risk plaque (HRP; 9.8% vs 2.8%; all $P < 0.05$; Table 2). MSU predicted HRP both unadjusted (odds ratio 3.81, 95% CI 1.27-11.40) and after adjustment for calcium, whether the Agatston score was entered as a continuous variable (4.19, 1.27-13.76) or dichotomised at 100 (4.91, 1.43-16.82); calcium itself carried no independent association with HRP in either model (adjusted odds ratio 0.54, 95% CI 0.12-2.37 for Agatston >100; Table 3). For obstructive disease, the hierarchy reversed: both markers contributed; calcium was the stronger correlate (adjusted odds ratio 7.88 for Agatston >100), while MSU remained independently predictive (3.22, 1.55-6.71).

Calcium indexes how much atherosclerosis is present; MSU indexes how likely it is to be unstable. Notably, MSU co-occurred with spotty calcification, itself a marker of active mineralisation rather than of the dense calcium that accompanies stabilization and quiescence[23,25], so the crystal marks lesions in an active biological state rather than the heavily calcified lesions. Because both signals derive from the same non-contrast acquisition, a single scan can separate the burden of atherosclerosis from its propensity to rupture.

Photon-counting CT corroborates coronary MSU with DECT

A single spectral technology, however capable, invites the concern that its material map is an algorithmic artefact. We therefore sought corroboration with photon-counting detector CT (PCCT), which reconstructs the energy of individual photons and so achieves spectral separation by a mechanism fundamentally different from dual-kVp acquisition. In an independent cohort of 92 consecutive patients (276 vessels) scanned on a dual-source photon-counting system, coronary MSU appeared as discrete intracoronary deposits, spectrally distinct from calcium and derivable from the routine non-contrast calcium-scoring acquisition at no additional radiation (Fig. 2E, F). MSU was identified in 12 of 92 patients (13.0%); 57 (61.9%) had none, and 23 (25.0%) harboured lesions that the deliberately conservative workflow could not confidently assign as urate or calcium (Supplementary Tables 1 and 2). As in the DECT cohort, MSU-positive patients were more often hypertensive (91.7% vs 59.6%) and diabetic (41.7% vs 8.8%) and carried a much higher calcium burden (median Agatston 218 vs 0), and high-risk plaque differed across the MSU-negative, MSU-positive and indeterminate groups (0%, 16.7% and 26.1%; P = 0.03).

Two caveats define what this cohort can and cannot show. With only 12 MSU-positive patients, it was powered to test whether a spectrally independent technology can detect the crystal, not to reproduce the HRP association; the indeterminate category reflects the conservative reading rather than a limitation of the detector: a lesion was called urate only when the spectral separation was unambiguous, so classifying indeterminate lesions as calcium yields the 13.0% floor, whereas including them (38.0%) approaches the DECT estimate of 35.3%. The essential point survives both readings: two detector technologies with fundamentally different physics converge on the same crystalline species, at comparable prevalence and with the same clinical associations, which is difficult to explain as a reconstruction artefact of two platforms.

Cross-polarised optics confirm coronary urate crystals

In fresh human coronary specimens, cross-polarised micro-optical coherence tomography (CP-μOCT) was employed to determine whether imaging identified a material with the spectral signature of urate, and whether it corresponded to genuine crystals. CP-μOCT resolved individual needle-shaped crystals within the intima in both cross-sectional and en-face views, and polarised-light microscopy of the same tissue revealed crystals with the strong negative birefringence that is the optical hallmark of MSU (Fig. 3). In prior work exploiting this contrast, uricase digestion abolished the birefringent needles, chemical proof of their identity as urate, and their counts tracked histological crystal burden and intimal thickening[26]. The specificity of this readout is worth emphasising: negative birefringence arises from the highly ordered, anisotropic lattice of monosodium urate and is not a property of the amorphous mineral of calcific plaque. Therefore, three methods resting on entirely different physical principles: dual-energy CT, photon-counting CT and cross-polarised optics converge on the same physical entity in the coronary wall.

Xanthine oxidase marks macrophages at the necrotic-core periphery and scales with plaque progression

Urate is the terminal product of xanthine oxidase (XO), so we mapped XO and macrophages across the full arc of human coronary lesion progression (67 lesions from 8 hearts): pathological intimal thickening (PIT) without and with macrophages, early and late fibroatheroma, and plaque rupture. Both macrophage (CD68) and XO immunoreactive area rose progressively across stages: CD68 from a median 0.25% of intimal area in macrophage-poor PIT to 6.14% at rupture, and XO from 0.33% to 1.90% (P for trend < 0.001 for each; Fig. 4A–C). Across all lesions, XO area was strongly correlated with macrophage area (Spearman $\rho = 0.85$, $P < 0.001$; Fig. 4d), and the correlation survived adjustment for lesion morphology (partial $\rho = 0.81$) and for the clustering of lesions within hearts (linear mixed-effects model, $\beta = 0.55$ per unit ln CD68, $P < 0.001$; within-heart ρ 0.28-0.93, median 0.76), consistent with $CD68^+$ macrophages as a cellular source of intimal XO.

XO, however, was not merely a function of macrophage density; it tracked necrotic-core formation. In a macrophage-rich PIT lesion, a dense band of $CD68^+$ cells expressed little XO (CD68 18.9% of intimal area, XO 0.9%; XO/CD68 ratio 0.05; Fig. 4E), whereas in early fibroatheroma XO and macrophages co-localised at the periphery of the necrotic core (CD68 5.4%, XO 2.5%; ratio 0.46; Fig. 4F), a near ten-fold shift in XO per macrophage as the core matured. With multiplex immunofluorescence, XO localised to $CD68^+$ macrophages in the deep intima abutting the necrotic core, with little XO in superficial macrophages, while $ACTA2^+$ smooth-muscle cells were confined to the media and fibrous cap, spatially separate from the intimal XO compartment (Fig. 5A). The XO-expressing cells were CD163-low and XO was sparse where reparative $CD163^+$ macrophages accumulated (Fig. 5B), defining a specific $CD68^+$/CD163-low subset rather than macrophages in general. A second, diffuse XO signal filled acellular regions of the necrotic core, lacking cellular outlines or nuclei, consistent with released enzyme retained on the extracellular matrix. Together, these data pinpoint a $CD68^+$/CD163-low macrophage population at the necrotic-core interface as a source of intra-plaque XO and, by extension, of local urate.

Two additional observations argue that this is a specific biological programme rather than a by-product of inflammation in general. First, the amount of XO per macrophage varied systematically between individuals: after accounting for macrophage burden, XO differed approximately 2.4-fold across hearts (random-intercept standard deviation 0.30 on the natural-log scale), indicating host-level determinants of urate-generating capacity superimposed on lesion stage. Second, the diffuse, cell-free XO pool within the core was most conspicuous at early fibroatheroma and waned toward rupture, the pattern expected if enzyme released from dying producer cells is captured on the extracellular matrix and then progressively lost as that matrix is degraded. Together with the phenotypic restriction to $CD68^+$/CD163-low cells and the exclusion of a smooth-muscle source, this places both the enzyme and its crystalline product precisely where the plaque is most prone to an event.

Discussion

Taken together, these observations relocate an old suspect. For decades, urate was judged by its blood concentration, found wanting in multivariable models, and dismissed as a bystander; our data shift the culprit from plasma to plaque. Three linked findings support this shift. First, non-contrast DECT resolves

monosodium urate within the coronary plaque and separates it from calcium and lipid, which single-energy CT cannot. Second, DECT-detected coronary MSU is an independent predictor of high-risk plaque, distinct from and complementary to the calcium score. Third, xanthine oxidase localizes to CD68⁺/CD163-low macrophages at the necrotic-core periphery, identifying a candidate cellular source of intraplaque urate. Photon-counting CT and cross-polarised optics, two distinct technologies, independently confirm the same physical entity.

This reframing dissolves the paradox that has long surrounded urate. In plasma, urate is an abundant antioxidant, which is why its circulating concentration is a poor guide to vascular harm; inside the macrophage, the xanthine-oxidase reaction that generates it is a potent source of superoxide and hydrogen peroxide[9], and XO-derived intracellular reactive oxygen species rather than soluble urate itself are the proximate trigger of NLRP3 activation and IL-1β release[27]. The same molecule is thus protective in the blood and pro-inflammatory in the wall, and only imaging of the deposited crystal, not measurement of the soluble pool, captures the pathogenic species.

The histopathology suggests a coherent producer-reservoir-release sequence. The producer is a CD68⁺/CD163-low intimal macrophage population at the necrotic-core periphery, distinguished by phenotype rather than location from the reparative CD163⁺ macrophages that share this region; its XO activity generates both reactive oxygen species and urate. Because macrophage XO raises intracellular urate that is not exported from intact cells[27], the crystalline deposits we observe cannot arise from simple secretion of soluble urate; the missing step is regulated cell death. Caspase 1-mediated gasdermin-D cleavage and pyroptotic membrane rupture can release accumulated cytosolic urate into the sodium-rich necrotic core, where MSU crystallises; and cleaved gasdermin-D and active Caspase 1 have been documented in macrophage-rich regions of human plaque, including our previous report[28–29]; in-situ demonstration of this step in coronary lesions is ongoing. Released IL-1β and MSU-stimulated macrophage products in turn activate the overlying endothelium[30]. The diffuse acellular XO within the core is consistent with high-affinity binding of released enzyme to matrix glycosaminoglycans[31–32]; its prominence at early fibroatheroma and decline toward rupture parallel matrix-metalloproteinase-mediated proteoglycan degradation as lesions advance[33–34]. MSU precipitates when the local product of urate and sodium concentrations exceeds solubility, favoured by high interstitial sodium, an acidic and hypoxic microenvironment, and matrix constituents that template nucleation, the same determinants that operate in the gouty joint[6]. This framework explains why coronary MSU appears only once a mature necrotic core has formed, concentrates at the core periphery, and can nucleate while the blood remains normouricaemic, reconciling the risk conferred by gout with the neutral cardiovascular results of serum urate lowering.

These findings extend, and qualitatively change, the small prior literature on vascular urate imaging. Earlier reports of DECT-detected coronary or cardiovascular MSU were confined to patients with established gout[13–16], in whom systemic supersaturation makes tissue deposition unsurprising and of uncertain relevance to the wider population. Here, in consecutive patients selected for suspected

coronary disease rather than gout and with serum urate in the normal range, coronary MSU was nonetheless present in roughly one in three and was tied specifically to the vulnerable phenotype. The phenomenon is therefore not a manifestation of clinical gout, but a common, previously unreported feature of coronary atherosclerosis, and the histopathology suggests how the crystal could be generated in situ by XO-expressing macrophages rather than deposited from the circulation, and why systemic urate is a poor guide to its presence.

Coronary MSU imaging is mechanistically distinct from existing vulnerable-plaque markers. CT high-risk features such as low attenuation and positive remodelling predict events[35] but describe plaque architecture; ^{18}F-sodium fluoride positron emission tomography localises active microcalcification[36]; and the perivascular fat-attenuation index reports pericoronary inflammation[37]. Coronary MSU instead images the crystalline product of macrophage xanthine-oxidase activity and inflammasome-driven cell death directly, and on photon-counting CT it is obtainable from the routine non-contrast calcium scan. This has practical consequences. Tens of millions of non-contrast, gated CT scans are already performed for calcium scoring; on photon-counting systems, the urate map is a reconstruction of raw data that already exists, and on dual-energy systems, it requires only a brief additional non-contrast series with no contrast medium, radiotracer, or catheterisation. Coronary MSU could therefore be reported alongside the calcium score to flag inflammation-active plaque at the population scale, complementing the calcium burden it accompanies, and doing so at a low cost and complexity.

The results reframe urate as a therapeutic target, treating a lesion rather than a number. Trials that lowered serum urate without regard to its site of deposition were neutral for cardiovascular outcomes[38–39]. Two mechanistically matched strategies follow. Xanthine-oxidase inhibition targets the producer, lowering both the urate substrate and the XO-derived reactive oxygen species that prime the inflammasome, and is conceptually distinct from uricosuric agents, which lower only the systemic pool. Anti-inflammatory therapy targets the sensor: interleukin-1β blockade with canakinumab reduced recurrent events independently of lipid lowering[40], and low-dose colchicine, which disrupts the microtubule scaffold required for inflammasome assembly[41–43]. Coronary MSU imaging could enrich such trials for patients who harbour the crystal and serve as a pharmacodynamic readout of whether therapy prevents or dissolves intraplaque deposits. This is the step that serum urate selection could not provide and that explains the neutral results of urate-lowering trials. An imaging-guided design with enrollment on the crystal, treatment with xanthine-oxidase inhibition, IL-1β blockade, or colchicine, and readout of the change in crystal burden would test the hypothesis directly and, if positive, convert coronary MSU from a marker of risk into an actionable therapeutic target.

A measure of caution is warranted before enthusiasm outruns evidence. Although reproduced across phantom, in vivo and photon-counting platforms, MSU and calcium occupy neighbouring rather than distant positions in spectral space, and their discrimination is most fragile precisely where it matters most: the small, sparse crystal aggregates of coronary plaque, where partial-volume averaging, cardiac motion and image noise can blur an already narrow margin. Our findings are therefore best read as an

inspiring and pathogenetically coherent hypothesis rather than a settled measurement; realising their promise will require larger and deliberately diverse cohorts, refined material decomposition algorithms, harmonised quantitative crystallisation metrics, and a therapeutic test of whether a coronary crystallisation score can be moved differentially by anti-inflammatory versus urate-directed therapy.

This study has additional limitations. The clinical cohorts were single-centre and modest in size, MSU was assessed qualitatively rather than quantitatively, and the cross-sectional design cannot establish the prognostic value of coronary MSU for incident events. A prospective urate-lowering imaging study has been initiated (S.F.). The PCCT cohort corroborates detectability but is not powered to replicate the HRP association, and formal concordance metrics with DECT are pending. The histopathology is cross-sectional autopsy material that cannot establish the temporal sequence linking XO upregulation, regulated cell death and crystallisation; intracellular urate was not directly visualised, and cleavage-specific Caspase 1 and gasdermin-D staining will be required to secure the pyroptotic-release step. Longitudinal imaging and functional XO or inflammasome inhibition will be needed to establish causality.

In summary, coronary monosodium urate is a detectable, mechanistically grounded imaging biomarker of crystal-driven sterile inflammation. It is common in patients without gout, forms locally and independently of systemic urate levels, specifically marks the vulnerable plaque, and identifies a rational population for anti-inflammatory and urate-directed therapy. More broadly, it invites a shift in how an old risk factor is understood from a soluble concentration measured in the blood to a crystalline lesion imaged in the wall. If a crystal that ignites the inflammasome can be seen noninvasively, quantified, and moved by therapy, then coronary MSU may become one of the first examples of imaging a specific, treatable driver of plaque instability, turning residual inflammatory risk from an abstraction into a target that can be found in an individual patient and followed over time.

Methods

Phantom study

An electron-density phantom (Sun Nuclear) containing rods of iodine (2, 5, 10 and 15 mg mL^{-1}), adipose, calcium (50, 100 and 300 mg mL^{-1}), MSU and solid water (Kyoto Kagaku) was scanned on a 320-detector-row system (Aquilion ONE ViSION, Canon Medical Systems) in dual-energy mode (80/135 kVp; tube-current modulation, target s.d. 28.0, 50–250 mA; 0.275-s rotation; 0.5-mm slices) and by single-energy CT at 120 kVp. Electron density and effective atomic number were derived on a dedicated workstation (Vitrea, Canon Medical Systems), and MSU was rendered by two-material (water/iodine) decomposition.

DECT study population

The clinical cohort was nested within a prospective coronary CT angiography (CCTA) extracellular-volume study; of 146 consenting patients, 30 were excluded (incomplete metabolic panel, n = 20; poor

image quality, n = 7; prior stents, n = 3), leaving 116 patients (348 vessels). The study was approved by the Juntendo University ethics committee (E21-0105) with an opt-out policy for the urate add-on.

DECT acquisition and MSU analysis

Non-contrast, ECG-gated DECT (80/135 kVp; 310 mA; 0.275-s rotation; 0.5-mm slices) preceded non-contrast single-energy CT for calcium scoring (120 kVp; 3.0-mm slices; AIDR 3D) and CCTA (100 kVp; 0.5-mm slices; 24.0 mg iodine kg^{-1} over 12 s). On the DECT workstation, electron density and effective atomic number were computed using the Spectral Analysis application, and MSU was identified using the Spectral Composition Analysis tool via two-material decomposition, with a region of interest defined by four coordinates in the water–iodine distribution.

CCTA analysis and plaque definitions

Calcium scoring and lesion assessment were performed with Ziostation2 (AMIN). Agatston scores were calculated per patient and per vessel; stenosis and plaque were graded by CAD-RADS 2.0[44]. Obstructive disease was ≥50% stenosis; positive remodelling, a remodelling index >1.1; low-attenuation plaque, non-calcified plaque <30 HU; and spotty calcification, a calcific focus ≤3 mm. High-risk plaque was defined as positive remodelling plus low attenuation[45].

Photon-counting CT

An independent cohort of 92 patients (276 vessels) with suspected coronary artery disease was imaged on a dual-source photon-counting detector CT system (Naeotom Alpha, Siemens Healthineers) at the Medical Imaging Centre, Semmelweis University (ethics IV/665-3/2022/EKU and BM/2497-1/2024). A non-contrast, ECG-gated calcium-scoring acquisition (high-pitch helical, 120 kVp, automated tube-current modulation, 144 × 0.4-mm detector, 0.25-s rotation) preceded contrast CCTA. Because photon-counting acquisition is inherently spectral, no separate dual-energy scan was required. Spectral post-processing datasets from the non-contrast acquisition were reconstructed at 70 keV, and MSU-positive lesions were identified on the syngo.via workstation (Kidney Stone and Gout applications, Siemens) using visual assessment and region-of-interest attenuation comparison; lesions that could not be confidently assigned were classified as indeterminate. Phantom and post-mortem coronary models, including a surgically removed uric-acid stone and a paraffin-embedded tophus, were used for calibration. This analysis was feasibility-oriented; no validated clinical workflow for coronary MSU quantification by PCCT yet exists.

Coronary histopathology

Human coronary specimens were obtained from the CVPath Institute autopsy registry (IRB RP-0175) and classified across the spectrum of plaque progression by a modified American Heart Association scheme with CT–pathology correlation[46]; lesion morphology was assigned on Movat pentachrome and haematoxylin–eosin sections, blinded to the quantitative data. Formalin-fixed, paraffin-embedded 5-μm

sections were stained by serial chromogenic immunohistochemistry for CD68 and CD163 and by two multiplex immunofluorescence panels (Panel 1: XO, CD68, ACTA2; Panel 2: XO, CD163; DAPI counterstain) on a Ventana Discovery Ultra platform. Antibodies were XO (Abcam ab109235, 1:1000), CD68 (Roche 790-2932, predilute), ACTA2 (Dako F3777, 1:500) and CD163 (Leica CD163-L-U, 1:100). Immunopositive area for CD68 and XO was quantified on whole-slide images (HALO, Indica Labs) within manually annotated intimal regions and expressed as a percentage of annotated area. For crystal detection, fresh unfixed coronary segments were embedded and cryosectioned for polarised-light microscopy under crossed polarisers with a first-order red compensator (formalin dissolves urate); MSU was identified by needle morphology and negative birefringence, and by cross-polarised micro-optical coherence tomography as previously described[26].

Statistics

Analyses used SPSS v23 (IBM) and R v4.4.2 (packages lme4, lmerTest and ggplot2), with two-sided $P < 0.05$. Normally distributed variables are shown as mean ± s.d., and others as median (interquartile range); groups were compared using the t-test or Mann–Whitney U test, and categorical variables using the χ^2 test. Associations of MSU with high-risk plaque and obstructive disease were tested by logistic regression (odds ratios with 95% confidence intervals). Trends in immunopositive area across ordered lesion categories were tested by the Jonckheere-Terpstra test; the XO–CD68 relationship was assessed by Spearman correlation, by partial Spearman correlation adjusted for lesion morphology, and by a linear mixed-effects model of ln(XO) on ln(CD68) with heart as a random intercept, fitted by maximum likelihood. Cluster-robust standard errors gave equivalent results, and between-heart variability is reported as the random-intercept standard deviation. No statistical method was used to predetermine sample size, and lesion morphology was assigned blindly to the quantitative immunohistochemical data.

Declarations

Acknowledgements

The study was supported by JSPS KAKENHI Grant Number 23K14849 to H.S., National Research, Development and Innovation Office (NKFIH), Hungary, grant K147355 to P.M-H., K. Lance Gould endowment fund (University of Texas Health, Houston) to J.N., and Harvey S. Rosenberg endowment fund (University of Texas Health, Houston) to N.N. We gratefully acknowledge Gargi Sharma, Kanwarpal Singh, Osman Ahsen, and Joseph A. Gardecki for their support of OCT imaging experiments.

Author contributions

J.N. designed and orchestrated the entire project plan. S.F. and H.S. designed and performed the dual-energy CT study and analysed the clinical data; P.M-H., L.S. and C.K.C. designed and performed the photon-counting CT study; R.V., N.N., A.V.F., A.F. and T.S. performed and interpreted the histopathology and morphometry; K.N. and G.J.T. performed the cross-polarised micro-OCT and polarised-light imaging; Y.O.K., N.T., Y.O.N., and Y.K. contributed to image acquisition and analysis. S.F., T.S., L.S., G.J.T., and J.N.

wrote the initial manuscript, and F.C., J.S., T.F.L., J-C.T., P.M.R. and T. M. contributed to data interpretation and multiple critical revisions of the manuscript. All authors approved the final version for submission to Nature Cardiovascular Research.

Competing interests

J.S.has received consultant fees from ROMTech, Atheneum, Clearview healthcare partners, Yale, Hulio, Horizon Pharmaceuticals/DINORA, ANI/Exeltis, USA Inc., Frictionless Solutions, Schipher, Crealta/Horizon, Medisys, Fidia, PK Med, Two labs Inc., Adept Field Solutions, Clinical Care options, Putnam associates, Focus forward, Navigant consulting, Spherix, MedIQ, Jupiter Life Science, UBM LLC, Trio Health, Medscape, WebMD, and Practice Point communications; the National Institutes of Health; and the American College of Rheumatology. J.S. has received institutional research support from Zimmer Biomet Holdings. J.S. received food and beverage payments from Intuitive Surgical Inc./Philips Electronics North America. J.S. owns stock options in Atyr pharmaceuticals, Atai life sciences, Kintara Therapeutics, Intelligent Biosolutions, Acumen pharmaceutical, TPT Global Tech, Vaxart pharmaceuticals, Atyu biopharma, Adaptimmune Therapeutics, GeoVax Labs, Pieris Pharmaceuticals, Enzolytics Inc., Seres Therapeutics, Tonix Pharmaceuticals Holding Corp., Aebona Pharmaceuticals, and Charlotte's Web Holdings, Inc. J.S. previously owned stock options in Amarin, Viking and Moderna pharmaceuticals. J.S. was on the speaker's bureau of Simply Speaking. J.S. was a member of the executive of Outcomes Measures in Rheumatology (OMERACT), an organization that develops outcome measures in rheumatology and receives arms-length funding from 8 companies. J.S. previously served on the FDA Arthritis Advisory Committee. J.S. previously served as a member of the following committees: member, the American College of Rheumatology's (ACR) Annual Meeting Planning Committee (AMPC) and Quality of Care Committees, the Chair of the ACR Meet-the-Professor, Workshop and Study Group Subcommittee and the co-chair of the ACR Criteria and Response Criteria subcommittee. J-C.T. has received research grants or research support from Amgen, Boehringer-Ingelheim, Ceapro, DalCor Pharmaceuticals, Merck, Novartis, Novo-Nordisk, and Verve Therapeutics. J-C.T. holds investments in DalCor Pharmaceuticals. J-C.T. has received personal compensation, including honoraria, consulting fees, advisory roles, or other professional income, from DalCor Pharmaceuticals, Merck, Pendopharm, and Zentiva. J-C.T. has been involved in intellectual property related to pharmacogenomics-guided CETP inhibition and the use of colchicine after myocardial infarction. J-C.T. has waived his rights to the colchicine patent and does not receive any financial benefit from it.

Funding

DECT work was supported by a JSPS KAKENHI Grant Number 23K14849 to H.S.; pathology studies at CVPath were supported by the K. Lance Gould Endowment of UTHealth to J.N.; photon-counting CT work was supported in part by the National Research, Development and Innovation Office (NKFIH), Hungary, grant K147355 to L.S. and P.M.-H. Additional funding sources to be confirmed.

Additional information

Supplementary information is available for this paper. Correspondence and requests for materials should be addressed to S.F.

Data availability

The data supporting the findings of this study are available from the corresponding author upon reasonable request. Individual patient imaging data are not publicly available because they contain information that could compromise participant privacy and are subject to the terms of the institutional ethics approvals.

Code availability

No custom code was generated for this study. Image analyses used commercially available software (Vitrea, Canon Medical Systems; syngo.via, Siemens Healthineers; Ziostation2, AMIN; HALO, Indica Labs), and statistical analyses used SPSS v23 and R v4.4.2 with the lme4 and lmerTest packages.

References

1. Libby, P. The changing landscape of atherosclerosis. Nature 592, 524–533 (2021).
2. Duewell, P. et al. NLRP3 inflammasomes are required for atherogenesis and activated by cholesterol crystals. Nature 464, 1357–1361 (2010).
3. Grebe, A., Hoss, F. & Latz, E. NLRP3 inflammasome and the IL-1 pathway in atherosclerosis. Circ. Res. 122, 1722–1740 (2018).
4. Clarson, L. E. et al. Increased cardiovascular mortality associated with gout: a systematic review and meta-analysis. Eur. J. Prev. Cardiol. 22, 335–343 (2015).
5. Zuo, T. et al. Hyperuricemia and coronary heart disease mortality: a meta-analysis of prospective cohort studies. BMC Cardiovasc. Disord. 16, 207 (2016).
6. So, A. K. & Martinon, F. Inflammation in gout: mechanisms and therapeutic targets. Nat. Rev. Rheumatol. 13, 639–647 (2017).
7. Martinon, F., Pétrilli, V., Mayor, A., Tardivel, A. & Tschopp, J. Gout-associated uric acid crystals activate the NALP3 inflammasome. Nature 440, 237–241 (2006).
8. Patetsios, P. et al. Identification of uric acid and xanthine oxidase in atherosclerotic plaque. Am. J. Cardiol. 88, 188–191 (2001).
9. Saito, Y., Tanaka, A., Node, K. & Kobayashi, Y. Uric acid and cardiovascular disease: a clinical review. J. Cardiol. 78, 51–57 (2021).
10. Primak, A. N. et al. Noninvasive differentiation of uric acid versus non-uric acid kidney stones using dual-energy CT. Acad. Radiol. 14, 1441–1447 (2007).
11. Choi, H. K. et al. Dual-energy CT in gout: a prospective validation study. Ann. Rheum. Dis. 71, 1466–1471 (2012).

12. Bongartz, T. et al. Dual-energy CT for the diagnosis of gout: an accuracy and diagnostic yield study. Ann. Rheum. Dis. 74, 1072–1077 (2015).
13. Klauser, A. S. et al. Dual-energy CT detection of cardiovascular monosodium urate deposits in patients with gout. JAMA Cardiol. 4, 1019–1028 (2019).
14. Feuchtner, G. M. et al. Monosodium urate crystal deposition in coronary artery plaque by 128-slice dual-energy CT: an ex vivo phantom and in vivo study. J. Comput. Assist. Tomogr. 45, 856–862 (2021).
15. Barazani, S. H. et al. Quantification of uric acid in vasculature of patients with gout using dual-energy CT. World J. Radiol. 12, 184–194 (2020).
16. Ren, H. et al. Detection of monosodium urate depositions and atherosclerotic plaques in the cardiovascular system by dual-energy CT. Heliyon 10, e24548 (2024).
17. Mach, F. et al. 2019 ESC/EAS guidelines for the management of dyslipidaemias. Eur. Heart J. 41, 111–188 (2020).
18. Arnett, D. K. et al. 2019 ACC/AHA guideline on the primary prevention of cardiovascular disease. J. Am. Coll. Cardiol. 74, 1376–1414 (2019).
19. Kawaguchi, Y. O. et al. Current status and future perspective of coronary artery calcium score in asymptomatic individuals. J. Cardiol. 85, 275–282 (2025).
20. Narula, J. & Strauss, H. W. The popcorn plaques. Nat. Med. 13, 532–534 (2007).
21. Morita, H. et al. Prevalence of CT-angiography-verified high-risk plaques and significant luminal stenosis in patients with zero coronary calcium score. Int. J. Cardiol. 158, 272–278 (2012).
22. Yu, Y. T. et al. Prevalence of coronary artery disease in symptomatic patients with zero coronary artery calcium score. Int. J. Cardiovasc. Imaging 37, 723–729 (2021).
23. van Rosendael, A. R. et al. Association of high-density calcified 1K plaque with risk of acute coronary syndrome. JAMA Cardiol. 5, 282–290 (2020).
24. Criqui, M. H. et al. Coronary artery calcium volume and density: the Multi-Ethnic Study of Atherosclerosis. JACC Cardiovasc. Imaging 10, 845–854 (2017).
25. Razavi, A. C. et al. Evolving role of calcium density in coronary artery calcium scoring and ASCVD risk. JACC Cardiovasc. Imaging 15, 1648–1662 (2022).
26. Nishimiya, K. et al. Imaging human coronary cholesterol/urate crystals with cross-polarized micro-optical coherence tomography. Front. Cardiovasc. Med. 11, 1433227 (2024).
27. Ives, A. et al. Xanthine oxidoreductase regulates macrophage IL-1β secretion upon NLRP3 inflammasome activation. Nat. Commun. 6, 7555 (2015).
28. Kolodgie, F. D. et al. Localization of apoptotic macrophages at the site of plaque rupture in sudden coronary death. Am. J. Pathol. 157, 1259–1268 (2000).
29. Puylaert, P. et al. Gasdermin D deficiency limits the transition of atherosclerotic plaques to an inflammatory phenotype in ApoE$^{-/-}$ mice. Biomedicines 10, 1171 (2022).

30. Chapman, P. T. et al. Endothelial activation in monosodium urate monohydrate crystal-induced inflammation. Arthritis Rheum. 40, 955–965 (1997).
31. Houston, M. et al. Binding of xanthine oxidase to vascular endothelium. J. Biol. Chem. 274, 4985–4994 (1999).
32. Houston, M. et al. Xanthine oxidase binding to glycosaminoglycans. Arch. Biochem. Biophys. 355, 1–8 (1997).
33. Newby, A. C. Metalloproteinase production from macrophages — a perfect storm leading to atherosclerotic plaque rupture. Exp. Physiol. 101, 1327–1337 (2016).
34. Otsuka, F. et al. Natural progression of atherosclerosis from pathologic intimal thickening to late fibroatheroma in human coronary arteries. Atherosclerosis 241, 772–782 (2015).
35. Motoyama, S. et al. Plaque characterization by coronary CT angiography and the likelihood of acute coronary events. J. Am. Coll. Cardiol. 66, 337–346 (2015).
36. Joshi, N. V. et al. ^{18}F-fluoride PET for identification of ruptured and high-risk coronary atherosclerotic plaques. Lancet 383, 705–713 (2014).
37. Oikonomou, E. K. et al. Non-invasive detection of coronary inflammation using CT and prediction of residual cardiovascular risk (CRISP-CT). Lancet 392, 929–939 (2018).
38. Kojima, S. et al. Febuxostat for cerebral and cardiorenovascular events prevention study (FREED). Eur. Heart J. 40, 1778–1786 (2019).
39. Mackenzie, I. S. et al. Allopurinol versus usual care in UK patients with ischaemic heart disease (ALL-HEART). Lancet 400, 1195–1205 (2022).
40. Ridker, P. M. et al. Antiinflammatory therapy with canakinumab for atherosclerotic disease. N. Engl. J. Med. 377, 1119–1131 (2017).
41. Tardif, J.-C. et al. Efficacy and safety of low-dose colchicine after myocardial infarction. N. Engl. J. Med. 381, 2497–2505 (2019).
42. Nidorf, S. M. et al. Colchicine in patients with chronic coronary disease. N. Engl. J. Med. 383, 1838–1847 (2020).
43. Samuel, M. et al. Long-term trials of colchicine for secondary prevention of vascular events: a meta-analysis. Eur. Heart J. 46, 2552–2563 (2025).
44. Cury, R. C. et al. CAD-RADS 2.0 — 2022 Coronary Artery Disease Reporting and Data System. J. Cardiovasc. Comput. Tomogr. 16, 536–557 (2022).
45. Shaw, L. J. et al. SCCT/NASCI expert consensus document on coronary CT imaging of atherosclerotic plaque. J. Cardiovasc. Comput. Tomogr. 15, 93–109 (2021).
46. Adachi, Y. et al. Coronary CT-based differentiation of pathologically verified fibroatheroma from pathologic intimal thickening. JACC Cardiovasc. Imaging https://doi.org/10.1016/j.jcmg.2026.04.011 (2026).

Tables

Table 1. Baseline characteristics of the DECT cohort.

Characteristic	Patients (n = 116)	Vessels (n = 348)
Age (years)	66.1 ± 11.5	—
Male, n (%)	65 (56.0)	—
Body-mass index (kg m^{-2})	23.8 (21.7, 26.2)	—
Hypertension, n (%)	63 (54.3)	—
Hyperlipidaemia, n (%)	26 (22.4)	—
Diabetes, n (%)	29 (25.0)	—
Current smoking, n (%)	15 (12.9)	—
eGFR (ml min^{-1} 1.73 m^{-2})	70.0 ± 17.4	—
Serum uric acid (mg dL^{-1})	5.2 ± 1.3	—
LDL-cholesterol (mg dL^{-1})	114.2 ± 31.3	—
Agatston score	40.9 (0, 227.1)	0 (0, 51.3)
Agatston score >100, n (%)	—	64 (18.4)
Obstructive CAD (≥50%), n (%)	32 (27.6)	58 (16.7)
Spotty calcification, n (%)	—	90 (25.9)
Low-attenuation plaque, n (%)	—	16 (4.6)
Positive remodelling, n (%)	—	26 (7.5)
High-risk plaque, n (%)	10 (8.6)	14 (4.0)

Data are mean ± s.d., median (interquartile range) or n (%). CAD, coronary artery disease; eGFR, estimated glomerular filtration rate.

Table 2. Characteristics by coronary MSU status (DECT).

Characteristic	MSU−	MSU+	P
Patients			
Age (years)	64.7 ± 11.1	68.5 ± 12.0	0.10
Male, n (%)	35 (46.7)	30 (73.2)	<0.05
Hypertension, n (%)	34 (45.3)	29 (70.7)	<0.05
Serum uric acid (mg dL^{-1})	4.9 ± 1.2	5.7 ± 1.4	<0.05
Agatston score	3.1 (0, 52.0)	302.3 (85.3, 855.0)	<0.05
Obstructive CAD, n (%)	9 (12.0)	23 (56.1)	<0.05
High-risk plaque, n (%)	5 (6.7)	5 (12.2)	0.32
Vessels			
Agatston score	0 (0, 15.6)	143.0 (46.7, 370.0)	<0.05
Agatston score >100, n (%)	30 (10.4)	34 (55.7)	<0.05
Obstructive CAD (≥50%), n (%)	30 (10.5)	28 (45.9)	<0.05
Spotty calcification, n (%)	63 (22.0)	27 (44.3)	<0.05
Low-attenuation plaque, n (%)	9 (3.1)	7 (11.5)	<0.05
Positive remodelling, n (%)	15 (5.2)	11 (18.0)	<0.05
High-risk plaque, n (%)	8 (2.8)	6 (9.8)	<0.05

Data are mean ± s.d., median (IQR) or n (%). MSU, monosodium urate.

Table 3. Vessel-level logistic regression for high-risk plaque and obstructive coronary artery disease.

Predictor	Univariable OR (95% CI)	P	Multivariable OR (95% CI)	P
High-risk plaque				
Agatston score (per 10)	1.004 (0.988, 1.010)	0.63	0.996 (0.974, 1.019)	0.71
Agatston score >100	1.221 (0.331, 4.508)	0.77	0.541 (0.124, 2.366)	0.54
Coronary MSU	3.805 (1.270, 11.399)	<0.05	4.911 (1.434, 16.815)	<0.05
Obstructive CAD				
Agatston score (per 10)	1.079 (1.054, 1.105)	<0.05	1.066 (1.040, 1.092)	<0.05
Agatston score >100	12.278 (6.442, 23.398)	<0.05	7.882 (3.902, 15.921)	<0.05
Coronary MSU	7.269 (3.872, 13.645)	<0.05	3.220 (1.545, 6.712)	<0.05

Multivariable models for high-risk plaque are adjusted for Agatston >100. OR, odds ratio; CI, confidence interval; CAD, coronary artery disease; MSU, monosodium urate.

Figures

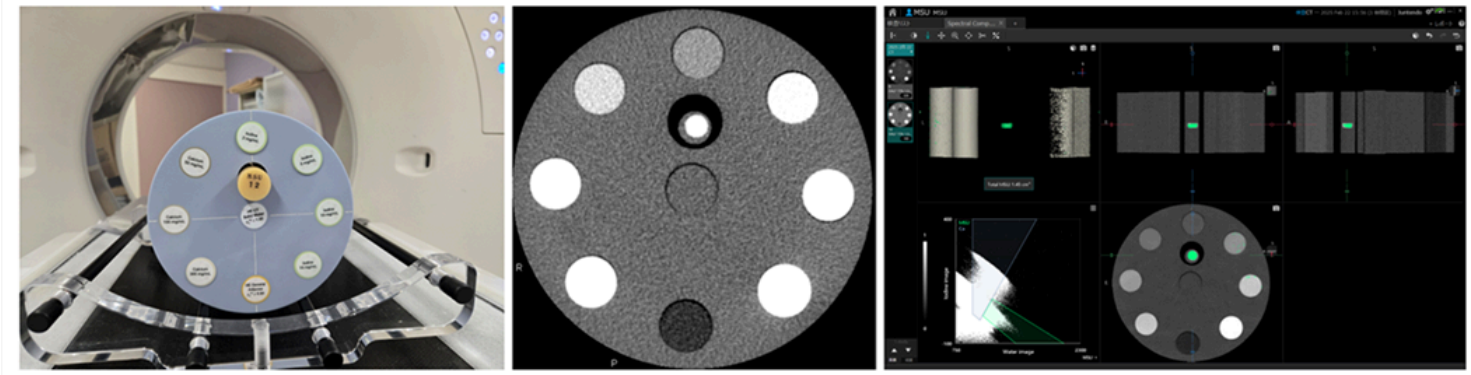

Figure 1

Phantom discrimination of monosodium urate by dual-energy CT. Electron-density phantom (left), single-energy CT image (centre) and DECT spectral-composition analysis with MSU shown as a green overlay (right). Rods: iodine (2, 5, 10, 15 mg mL⁻¹), adipose, calcium (300, 100, 50 mg mL⁻¹), MSU and solid water. Tabulated 120-kVp attenuation, electron density and effective atomic number are given in the text.

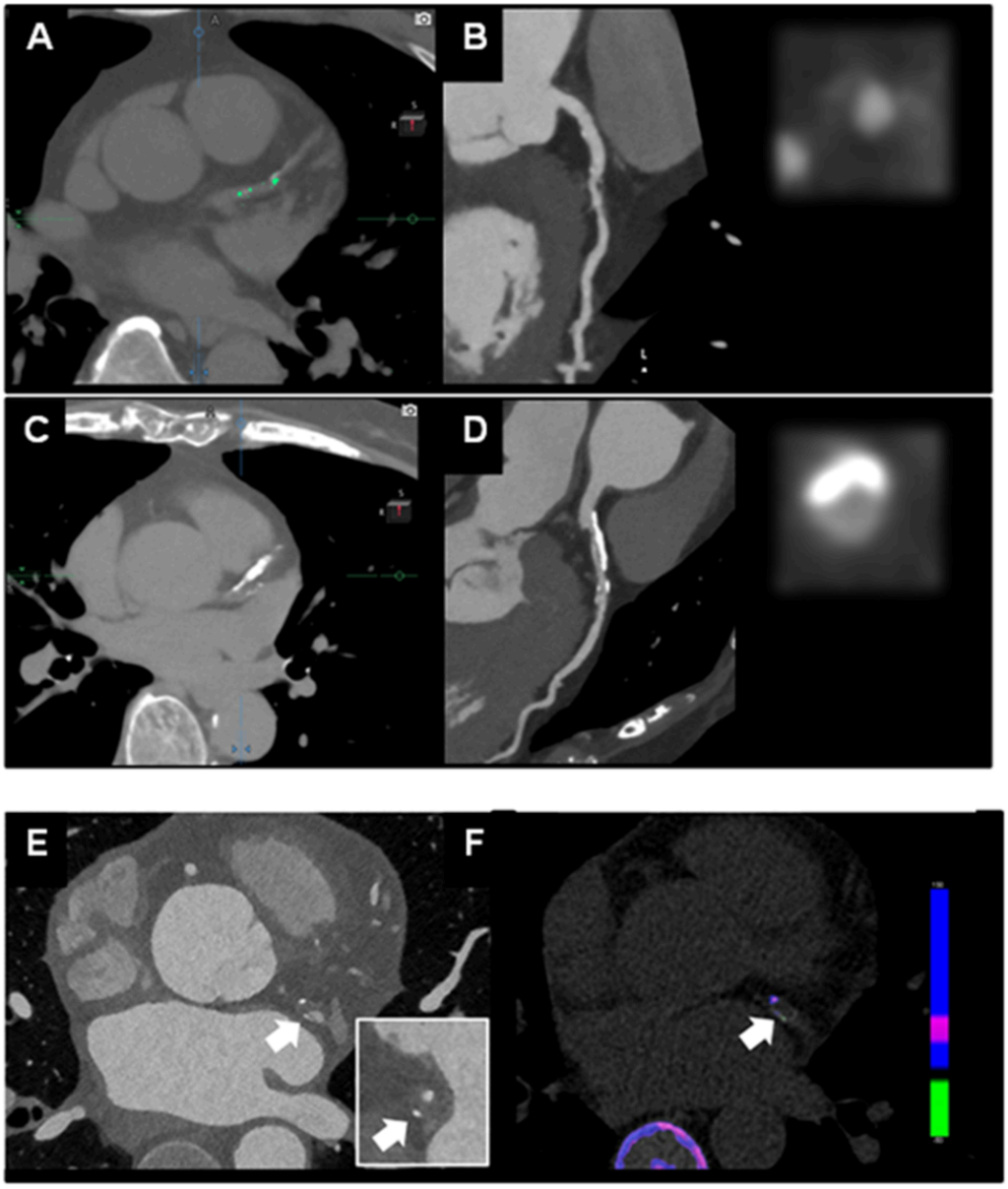

Figure 2

In vivo coronary monosodium urate imaged by dual-energy and photon-counting CT. A, Non-contrast, ECG-gated dual-energy CT of a coronary segment, with MSU shown as a spectral overlay distinct from adjacent calcium, in a hypertensive, hypercholesterolemic man with uric acid 7.8 mg/dl (165cm, 78kg, BMI 28.7). B, Contrast-enhanced coronary CT angiography demonstrates a high-risk plaque (arrow) at the same location. C, Corresponding images from a hypertensive, hypercholesterolemic woman with serum urate 5.9 mg/dl (149cm, 44kg, BMI 19.8) show no urate deposits in coronary arteries (left) and D, stable calcified plaque on CT angiography (right). E-F, Photon-counting CT spectral reconstruction of the

lesion, with MSU rendered in green and calcium in purple. Two spectrally independent technologies detect the same intracoronary crystal.

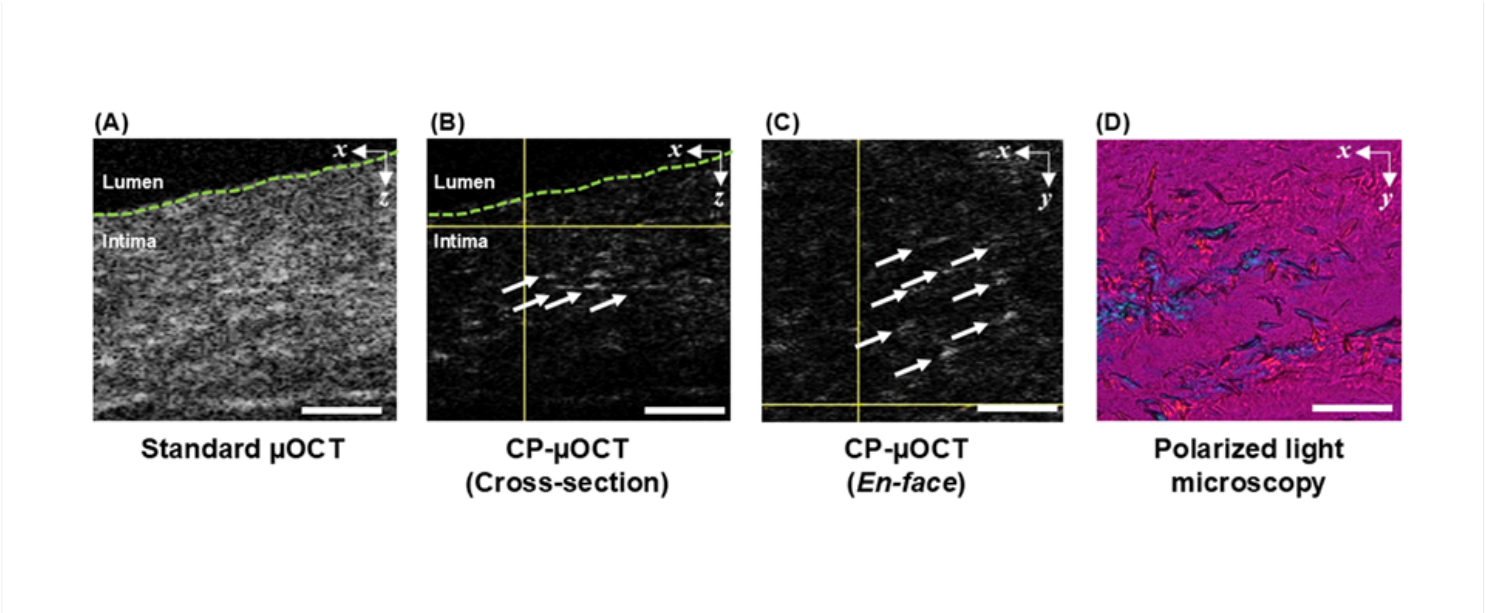

Figure 3

Cross-polarised micro-OCT and polarised-light microscopy of coronary crystals. Standard μOCT (a), cross-sectional (b) and en-face (c) cross-polarised μOCT (CP-μOCT), and polarised-light microscopy (d) of a fresh human cadaver coronary artery. Cross-sectional and en-face CP-μOCT show accumulated needle-shaped crystals (arrows); polarised-light microscopy of the same specimen shows crystals with negative birefringence characteristic of MSU. Scale bars, 50 μm.

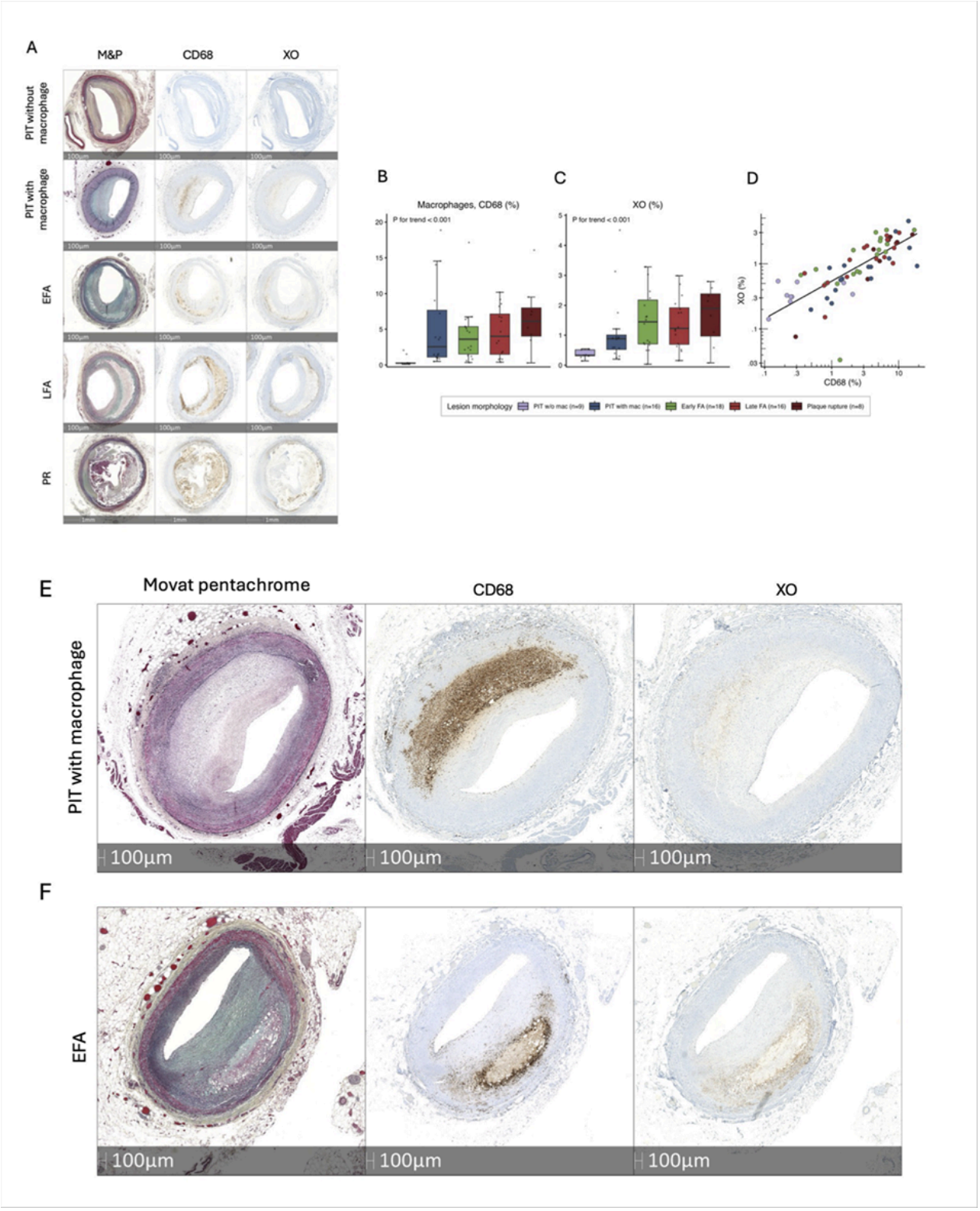

Figure 4

Xanthine oxidase parallels macrophage burden across plaque progression and emerges with necrotic core formation. a, Representative serial sections of human coronary lesions: PIT without macrophages, PIT with macrophages, early fibroatheroma (EFA), late fibroatheroma (LFA) and plaque rupture (PR), stained with Movat pentachrome and by immunohistochemistry for CD68 and xanthine oxidase (XO). b,c, $CD68^+$ macrophage area (b) and XO^+ area (c) as a percentage of annotated intimal area across lesion

morphology (n = 9, 16, 18, 16 and 8 lesions; 67 lesions from 8 hearts); boxes show median and interquartile range, whiskers extend to 1.5 × IQR, individual lesions overlaid; P for trend by the Jonckheere-Terpstra test. d, XO versus CD68 area across all lesions (log-log axes; line, least-squares fit; Spearman ρ = 0.85, P < 0.001; mixed-effects model with heart as a random intercept, β = 0.55, P < 0.001). e,f, Two lesions from one heart: PIT with macrophages (e), with dense CD68⁺ macrophages but sparse XO (CD68 18.9%, XO 0.9%; ratio 0.05), and early fibroatheroma (f), with CD68⁺ macrophages and XO co-localised at the necrotic-core periphery (CD68 5.4%, XO 2.5%; ratio 0.46).

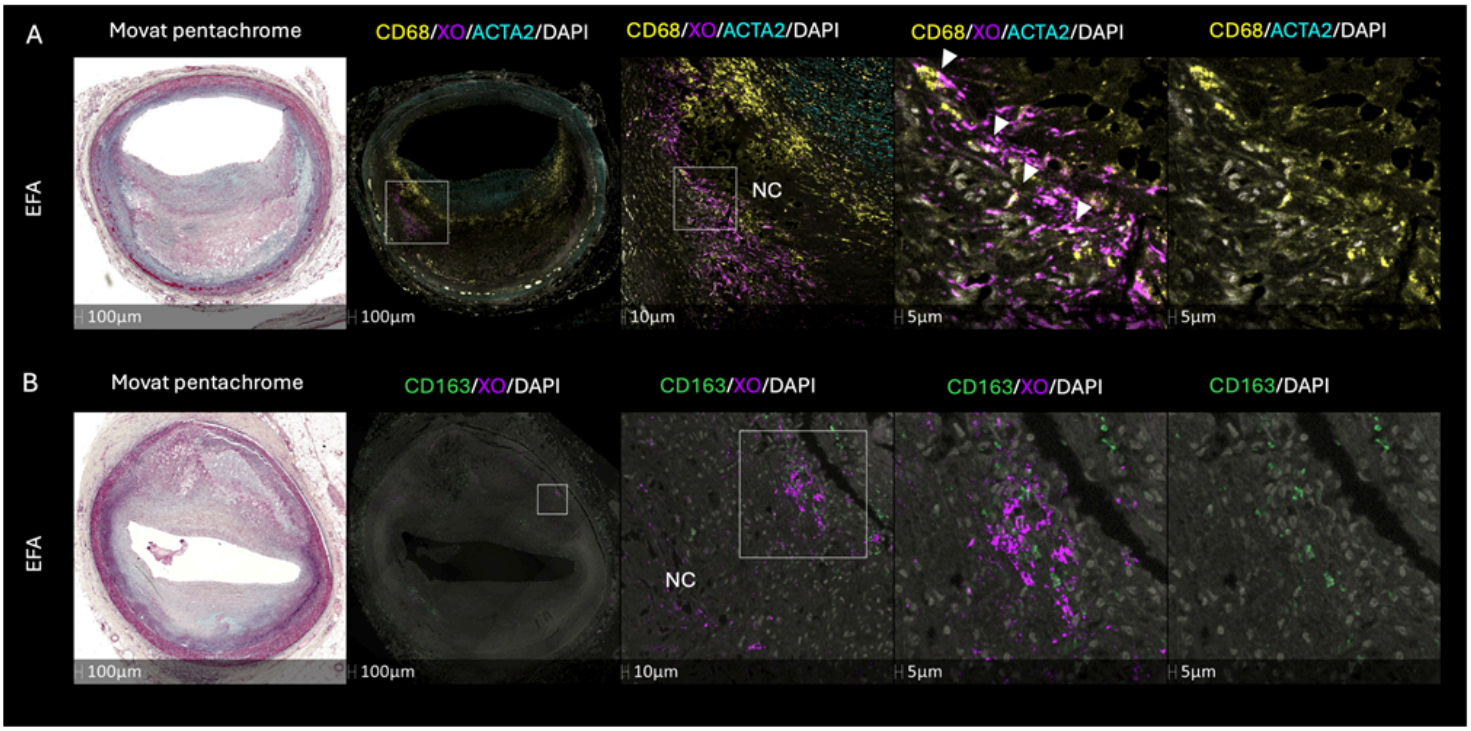

Figure 5

XO is expressed by CD68⁺, CD163-low macrophages at the necrotic-core periphery. a, Early fibroatheroma stained with Movat pentachrome (left) and by multiplex immunofluorescence for CD68 (yellow), XO (magenta), ACTA2 (cyan) and DAPI (white). Boxed regions are shown at higher magnification to the right; the final panel omits the XO channel. Arrowheads indicate CD68⁺ macrophages co-expressing XO at the necrotic-core periphery; ACTA2⁺ smooth-muscle cells are present in the media and fibrous cap. b, Early fibroatheroma stained with Movat pentachrome (left) and for CD163 (green), XO (magenta) and DAPI (white), presented as in a; CD163⁺ macrophages accumulate at the necrotic-core periphery but show little XO. NC, necrotic core; EFA, early fibroatheroma.

Supplementary Files

This is a list of supplementary files associated with this preprint. Click to download.

- SupplementaryTables.docx